



Effect of Cu substitution on the structural, magnetic, and dc electrical resistivity response of $\text{Co}_{0.5}\text{Mg}_{0.5-x}\text{Cu}_x\text{Fe}_2\text{O}_4$ nanoferrites

P. Himakar¹ · K. Jayadev¹ · D. Parajuli¹ · N. Murali² · Paulos Taddesse³ · S Yonatan Mulushoa⁴ · Tulu Wegayehu Mammo⁵ · B. Kishore Babu⁶ · V. Veeraiah¹ · K. Samatha¹

Received: 17 November 2020 / Accepted: 13 April 2021 / Published online: 24 April 2021
© The Author(s), under exclusive licence to Springer-Verlag GmbH, DE part of Springer Nature 2021

Abstract

$\text{Co}_{0.5}\text{Mg}_{0.5-x}\text{Cu}_x\text{Fe}_2\text{O}_4$ ($x=0.0, 0.2$ and 0.4) nanoferrites were prepared by sol–gel auto combustion method. XRD, FT-IR, and HRTEM studies revealed the single-phase spinel cubic crystal structure of all samples with Fd-3 m space group. The lattice constant, calculated using the XRD data, was found in the range 8.3936–8.4735 Å. The average crystallite sizes were found to be in the range of between 38.8 and 49.9 nm. The microstructural behavior and elemental composition of all samples were detected by FE-SEM and EDS, respectively. FTIR curves showed two absorption bands ν_1 with higher frequency and ν_2 with a lower frequency, indicating metal cation and oxygen bond stretching at tetrahedral and octahedral sites. DC resistivity was decreased with increasing the content of copper. VSM study confirmed the ferrimagnetic behavior of all samples. The values of remnant ratios obtained from VSM data showed their isotropic nature forming single domains ferrimagnetic particles

Keywords Sol-gel auto-combustion · Nanoferrite · XRD · VSM · Ferrimagnetic

1 Introduction

The ferrites are ceramics materials made up of a large amount of Fe_2O_3 blended with a small number of other elements like barium, cobalt, manganese, nickel, and zinc [1]. Their ferrimagnetic behavior is famous for making permanent magnet used in refrigerator, loudspeakers, electric motors, etc., due to their high coercivity or difficulty of demagnetizing and termed as hard ferrites and in high-frequency inductors, transformers, antennas, microwave

components, etc., due to their low coercivity or easily demagnetize and termed as soft ferrites [2–4]. At the same time, cobalt ferrites are hard ferrites. Many ferrites have spinel structures in the form of AB_2O_4 , A, and B are metal cations. ‘A’ cation covers 1/8th of the holes belonging to tetrahedral positions, and ‘B’ cations include 1/2 of the octahedral holes, i.e., $\text{A}^{2+}\text{B}_2^{3+}\text{O}_4^{2-}$. Cobalt ferrites (CoFe_2O_4) are hard ferrimagnetic materials. They are accessible to synthesis and have a simple structure for analysis. They have sizeable magnetocrystalline nature, wider coercivity, medium magnetic saturation, chemically stable, mechanically strong, and high electrical resistivity [5–7]. The spinel-type ferrites are set up in various biomedical, catalysis, wastewater purification, and industries [8].

In contrast, MgFe_2O_4 ferrite is a soft one with a magnetic moment lower than other spinel ferrites [9]. Here, Mg^{2+} ions want to stay in the octahedral site and have no magnetic moment. Few magnetic anisotropies are consequently the occurrence of Fe^{3+} ions.

The saturation magnetization and real part of permeability increase when divalent magnetic cations like Co, Ni, etc., are substituted by non-magnetic cations like Mg, Cu, etc., up to 50%. The allocation of the cations in the sample is greatly affected by the synthesis procedure [10]. These days, researchers employ various synthesis techniques

✉ N. Murali
muraliphda@gmail.com

¹ Department of Physics, College of Science and Technology, Andhra University, Visakhapatnam, India

² Department of Engineering Physics, AUCE (A), Andhra University, Visakhapatnam, Andhra Pradesh, India

³ Department of Physics, College of Natural Science, Arba Minch University, Arba Minch, Ethiopia

⁴ Department of Physics, Wolkite University, Wolkite, Ethiopia

⁵ Department of Physics, CNCS, Aksum University, Axum, Ethiopia

⁶ Department of Engineering Chemistry, A. U. College of Engineering (A), Andhra University, Visakhapatnam, India

such as sol–gel auto-combustion technique among hydrothermal, co-precipitation, electrodeposition, glass crystallization, solid-state reaction technique, and solvothermal, ultrasonic spray pyrolysis and microemulsion, etc. [11–13]. The sol–gel auto-combustion method is more comfortable, efficient, and faster than others for producing a large amount of homogeneous product [14].

In the present work, sol–gel auto-combustion method was utilized to make $\text{Co}_{0.5}\text{Mg}_{0.5-x}\text{Cu}_x\text{Fe}_2\text{O}_4$ (at $x = 0.0, 0.2$ and 0.4) nanoferrites. The structural, morphological, magnetic, and dc resistivity properties of all nanoferrites were investigated using advanced characterization techniques. This is the first report about $\text{Co}_{0.5}\text{Mg}_{0.5}\text{Fe}_2\text{O}_4$, $\text{Co}_{0.5}\text{Mg}_{0.3}\text{Cu}_{0.2}\text{Fe}_2\text{O}_4$, and $\text{Co}_{0.5}\text{Mg}_{0.1}\text{Cu}_{0.4}\text{Fe}_2\text{O}_4$ nanoferrites synthesized by the sol–gel auto-combustion method to the knowledge of the authors.

2 Experimental details

Cobalt nitrate hexahydrate of analytical grade of 99% purity [$\text{Co}(\text{NO}_3)_2 \cdot 6\text{H}_2\text{O}$], zinc nitrate hexahydrate [$\text{Zn}(\text{NO}_3)_2 \cdot 6\text{H}_2\text{O}$], nickel nitrate [$\text{Ni}(\text{NO}_3)_2 \cdot 6\text{H}_2\text{O}$], magnesium nitrate hexahydrate [$\text{Mg}(\text{NO}_3)_2 \cdot 6\text{H}_2\text{O}$], ferric nitrate [$\text{Fe}(\text{NO}_3)_3 \cdot 9\text{H}_2\text{O}$] are mixed with the same grade of citric acid monohydrate [$\text{C}_6\text{H}_8\text{O}_7 \cdot \text{H}_2\text{O}$] in 1:1 M ratio. The primary function of citric acid is to segregate metal ions, make a homogeneous colloidal solution and reduce the preparation temperature. The interaction between oxygen and metal ions controls the precipitation of metal nitrates during water dehydration. The addition of ammonia neutralizes the mixed solution to pH-7 and supports forming a gel by increasing the solubility of metal ions. The distilled water is added to the metal nitrates at their optimal to make a clear solution. The resultant is stirred continuously at around 150°C for the gel formation. The excess water in the gel is dried generally to remove excess water and powdered finely by agate mortar and pestle. The powder is sintered for 3 h continuously at 1000°C . The disk-shaped pellets are made ready after subjecting the powder to 5 tons of pressure.

The structural data, including lattice parameters and crystallite size of the ferrite sample, were examined with XRD (PANalytical XPert PRO diffractometer with 1.5402 \AA $\text{CuK}\alpha$ radiation step size of 0.008). The morphology and chemical compositions were studied with Scanning Electron Microscope (Carl Zeiss, EVOMA 15, Oxford Instruments, Inca Penta FETx3.JPG instrument) and attached Electron Dispersive X-ray (EDX). Transmission Electron Microscopy (TEM) (Hitachi H-8100) the accelerating TEM voltage was nearly 200 kV. FTIR (IR Prestige21 Shimadzu) confirms the chemical and structural changes. VSM (1T) at room temperature gives the

Magnetic measurements. DC electrical resistivity was estimated, employing two probe procedures in the temperature range of 30°C and 215°C .

3 Result and discussion

The X-ray diffraction pattern of $\text{Co}_{0.5}\text{Mg}_{0.5-x}\text{Cu}_x\text{Fe}_2\text{O}_4$ ($x = 0.0, 0.2$ and 0.4) powdered nanoferrites sintered at 1000°C for 3 h brought about via sol–gel technique with auto-combustion is displayed in Fig. 1. Every peak is indexed about the standard pattern JCPDS card Nos. 79–1744 and 73–2410 for the nanoferrites CoFe_2O_4 and MgFe_2O_4 , respectively, and found to be (220), (311), (400), (442), (511), and (440) [15]. These indexes represent reflections belonging to the f.c.c cubic structure. Other than these reflections, no additional phases were recorded in the XRD pattern. The patterns are indexed with all the planes indicative of spinel cubic crystal structure with the space group of Fd-3 m.

The phase and lattice parameter of the sample was identified by the powder X-ray diffraction method. The intensity of the diffracted beam and the angle of diffraction in terms of angular width (2θ) in the range 10° – 70° are as shown in the figure. In the figure, the sharp and narrower peaks show that the sample has a high crystalline nature. Also, the shifting of peaks toward the lower value of 2θ with the rise in the density of Cu reveals the respective increment of the lattice parameter.

The X-ray diffraction pattern (311) gives the crystallite size using an online calculator. The lattice parameter, a , of the $\text{Co}_{0.5}\text{Mg}_{0.5-x}\text{Cu}_x\text{Fe}_2\text{O}_4$ powder samples is calculated with the following relation [16]:

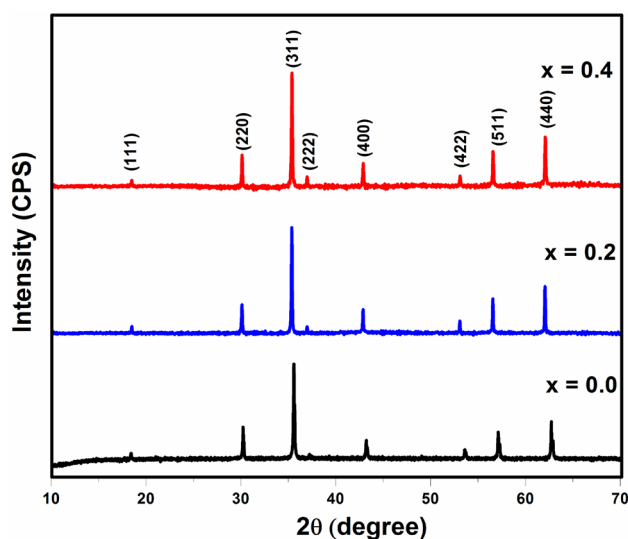


Fig. 1 XRD design considered for $\text{Co}_{0.5}\text{Mg}_{0.5-x}\text{Cu}_x\text{Fe}_2\text{O}_4$ nanoferrites

$$a = d\sqrt{h^2 + k^2 + l^2} \tag{1}$$

where d represents interplanar spacing for the (hkl) plane, values of θ and d are obtained from the experiment based on Bragg’s diffraction law.

The lattice parameters estimated are tabulated in Table 1. The ionic radius of Cu^{2+} (0.73 Å) is more significant than that of Mg^{2+} (0.72 Å). So, the lattice constant after doping with Cu^{2+} increases [17]. The graph between lattice constant a of $\text{Co}_{0.5}\text{Mg}_{0.5-x}\text{Cu}_x\text{Fe}_2\text{O}_4$ ($x=0.0, 0.2$ and 0.4) and Cu density (x) is as shown in Fig. 2.

The maximum peak from the XRD pattern (311) is considered for the calculation of crystallite size with the help of a calculator depending on Scherer’s formula. The more significant separation of diffraction peaks (Fig. 1) indicates a smaller crystallite size of the samples. The broadness of the peak decreases with increasing Cu content which shows increasing crystallite size. Scherer’s formula is given as [18]:

$$D_{311} = \frac{0.9\lambda}{\beta\cos\theta} \tag{2}$$

where D_{311} is the crystallite size, λ denotes X-ray wavelength exactly of 1.5406 Å, β represents full width at half maximum (FWHM) of (311) peak, and θ symbolizes angle of diffraction. $\beta = \sqrt{\beta_{\text{exp}}^2 - \beta_{\text{inst}}^2}$ is the FWHM in radians where β_{exp} is the experimental FWHM and β_{inst} is the instrumentation broadening factor. Its value is 0.06° for silicon powder used as a standard sample. The peak (311) obtained by Gaussian profile fit and crystallite size of samples under consideration are revealed in Fig. 1. The plot between crystallite size and Cu concentration (x) of $\text{Co}_{0.5}\text{Mg}_{0.5}\text{Fe}_2\text{O}_4$ samples is displayed in Fig. 2.

As we have seen from Fig. 2, lattice constant increases and then decreases, but crystallite size always increases with Cu^{2+} concentration increasing. The lattice parameter is observed to increase up to $x=0.2$, and for higher copper concentrations, it decreases. An increase in the lattice constant with increasing copper concentration is expected because of the large ionic radius of Cu^{2+} (0.73 Å) compared to that of Mg^{2+} (0.72 Å). Thus, the decrease in a for $x>0.2$ may be due to the transfer of Co^{2+} ions from octahedral sites to tetrahedral sites without bringing phase change because of the increased concentration of copper ions [19]. Additionally, the lattice parameter does not depend on ionic radii alone

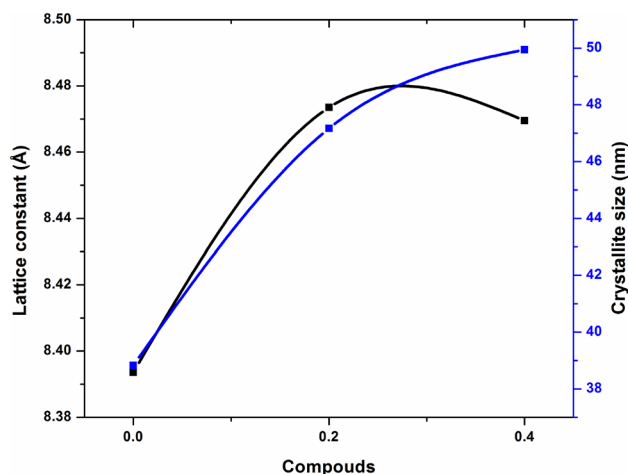


Fig. 2 Variation of lattice constant and crystallite sizes with Cu concentration for $\text{Co}_{0.5}\text{Mg}_{0.5-x}\text{Cu}_x\text{Fe}_2\text{O}_4$ nanoferrites

but also the contributions from many other factors such as the long-range attractive Coulomb forces, bond length, etc. The proportion increase in crystallite size may be due to the uniform distribution of Mg and Cu ions. The calculated crystallite sizes are in the range of 38.83 to 49.94 nm.

The FESEM gives images of the physical texture and morphology of $\text{Co}_{0.5}\text{Mg}_{0.5-x}\text{Cu}_x\text{Fe}_2\text{O}_4$ ($x=0.0, 0.2$, and 0.4) of the mixed ferrite material. The images are as shown in Fig. 3. In the figures, the crystal grains are clear and inhomogeneous in shape and size. The decrease in agglomeration with a concentration of Cu^{2+} may be due to non-magnetic dopant addition in place of magnetic cations, and the synthesis condition [20]. The pores and voids are created after releasing gases in the synthesis process.

The value of the grain size of $\text{Co}_{0.5}\text{Mg}_{0.5-x}\text{Cu}_x\text{Fe}_2\text{O}_4$ samples is listed in Table 1. Here, the grain size increases with increasing Cu concentration. Since Cu has a larger ionic radius than Mg, there is a more considerable volume expansion by which the density of X-rays is lowered. Nevertheless, the bigger atomic weights of Cu overcome the volume expansion and reduce the density [21]. As a result, the grain size keeps increasing.

The increase in Cu concentration in each synthesized sample and its percentage of the elemental composition is shown by the EDS spectra, as shown in Fig. 4a to d. Histogram for elemental weight composition is shown in Fig. 5,

Table 1 Structural parameters for $\text{Co}_{0.5}\text{Mg}_{0.5-x}\text{Cu}_x\text{Fe}_2\text{O}_4$ nanoferrites

Composition (x)	Lattice constant (Å)	Cell Volume (Å ³)	Crystallite size (nm)	Space group	Grain size (µm)
0.0	8.394	591.3541	38.83	Fd-3 m	0.45
0.2	8.474	608.3949	47.17	Fd-3 m	0.50
0.4	8.469	607.4015	49.94	Fd-3 m	0.55

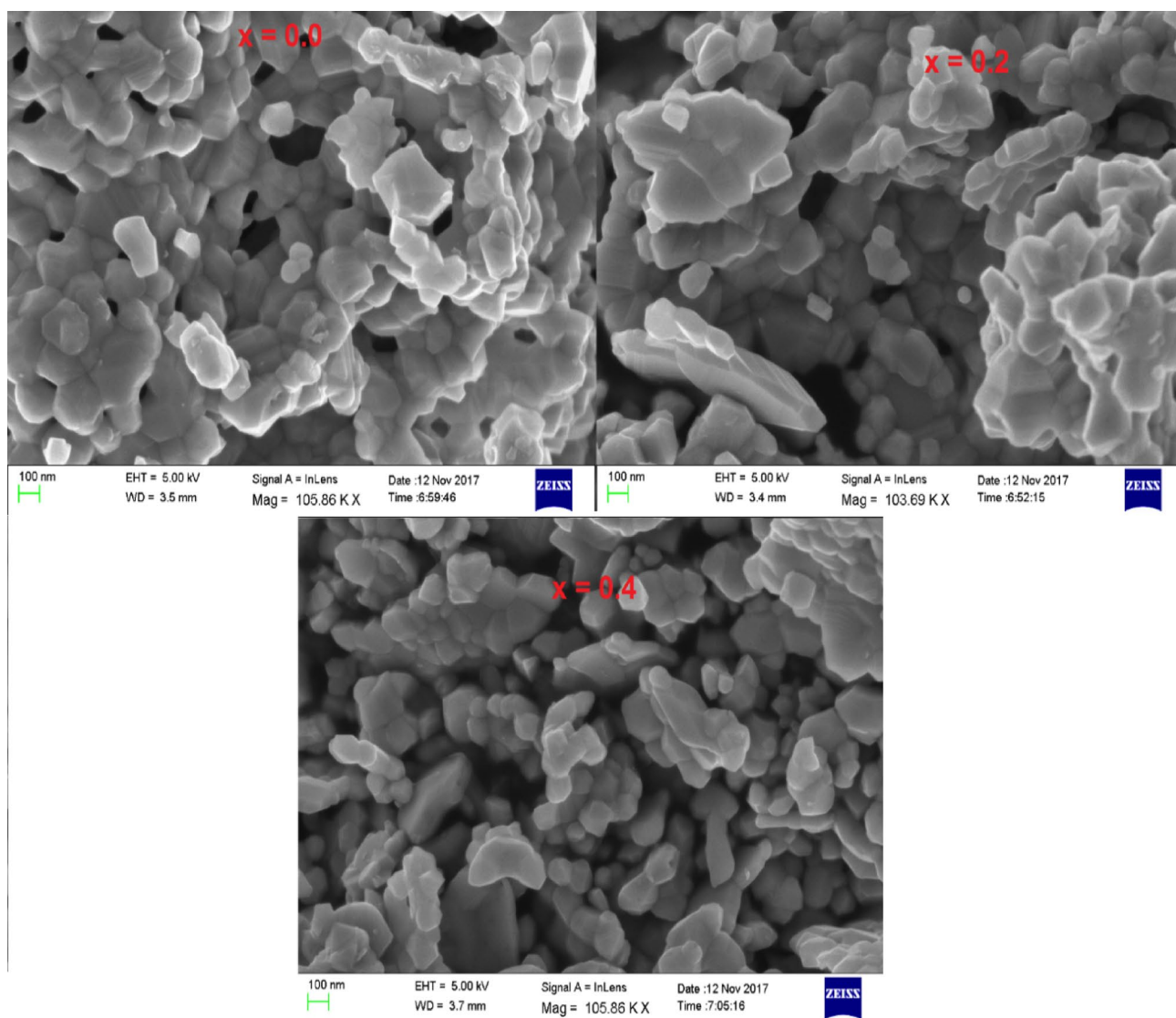


Fig. 3 SEM images of $\text{Co}_{0.5}\text{Mg}_{0.5-x}\text{Cu}_x\text{Fe}_2\text{O}_4$ nanoferrites

and it is listed in Table 2. It agrees with the stoichiometric composition. The spectra have shown the appropriate ratios.

The morphology and structure of the prepared $\text{Co}_{0.5}\text{Mg}_{0.5-x}\text{Cu}_x\text{Fe}_2\text{O}_4$ ($x=0.0$ and 0.2) ferrite samples are confirmed by HRTEM as shown in Figs. 6a to c and 7a to c. The results agreed well with the previous ones [22]. The selected area electron diffraction (SAED) gives the spotty ring pattern with cubic structure nanoferrite [23]. The particle sizes decreased with increasing Cu content. Mean particle size and interplanar distance d from HRTEM and crystallite size and d from XRD agree well. Similarly, the SAED ring pattern of the samples resolved at (220), (311), (400), (422), (511), (440) reflections agrees with that in the XRD pattern.

It helps to identify the chemical functional group analytically in both liquid and solid phases. The specific feature

creates infrared absorption due to the molecule's electric dipole moment change due to its bond's expansion and contraction. The infrared spectra of $\text{Co}_{0.5}\text{Mg}_{0.5-x}\text{Cu}_x\text{Fe}_2\text{O}_4$ sample for the concentrations ($x=0.0, 0.2$ and 0.4) are as shown in Fig. 8. The two strong absorption bands are seen on the IR curve in Fig. 8 of sintered powder. The two bands ν_1 with higher frequency (octahedral complexes) and ν_2 with lower frequency (tetrahedral complexes) indicate that metal cation and oxygen bond stretching $\text{M}_{\text{tetra}} \leftrightarrow \text{O}$ and $\text{M}_{\text{octa}} \leftrightarrow \text{O}$ with respective force constants K_t and K_o at tetrahedral and octahedral sites, respectively [24, 25]. Their values are tabulated in Table 3.

The vibrating sample magnetometer (VSM) is utilized to find the magnetic properties of a material. Their hysteresis loops for respective concentrations obtained from VSM under the field of $\pm 10,000$ Oe are shown in Fig. 9.

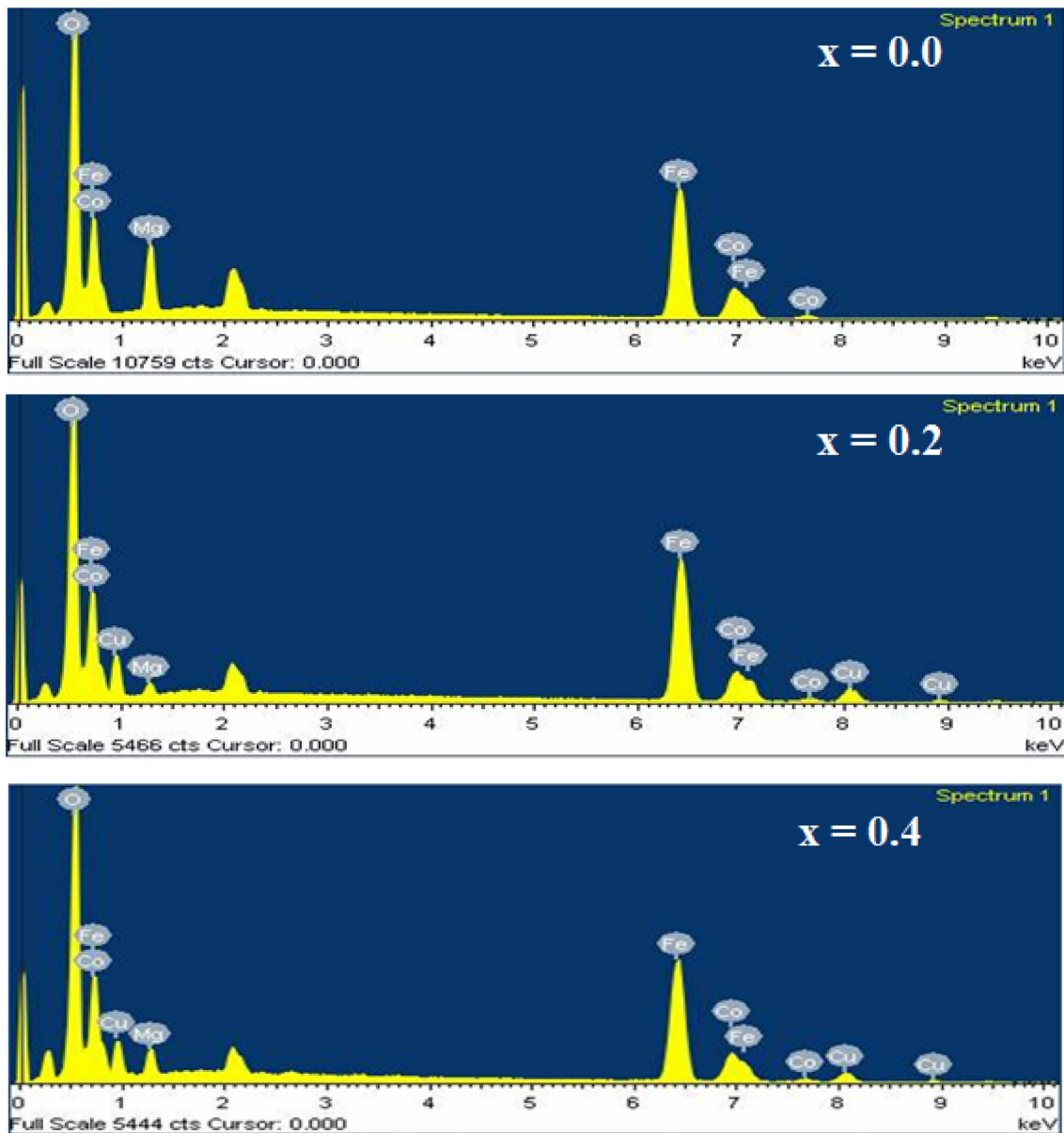


Fig. 4 EDS spectra of $\text{Co}_{0.5}\text{Ni}_{0.5-x}\text{Cu}_x\text{Fe}_2\text{O}_4$ nanoferrites

The S-shaped hysteresis loop indicates that the sample is ferromagnetic, and the higher coercive value of these samples indicates them as hard ferrimagnetic ferrites [26, 27]. Higher the retentivity (lower coercivity), it is more strongly magnetized and more rapidly loses its magnetism. The magnitude of saturation magnetization first rises, becomes maximum and again declines with increasing Cu concentration. The exchange interaction between the ions belonging to tetrahedral and octahedral positions may cause this effect. The particle and magnetic domain size reduction decreases the coercivity and hence H_c [28–30].

The measured values of saturation and remnant magnetization (M_s and M_r), coercive field (H_c), the experimental

and theoretical importance of Bohr magneton (μ_B), and anisotropy constant (K) of $\text{Co}_{0.5}\text{Mg}_{0.5-x}\text{Cu}_x\text{Fe}_2\text{O}_4$ samples of all concentrations are in Table 4.

The remnant ratio ($R = M_r/M_s$) below 0.5 shows the isotropic nature of the materials forming single domain ferrimagnetic particles [31]. Ferrites have high M_s and moderate H_c [18] required for magnetic recording media [32]. It is clear from Fig. 10 shows that saturation, remnant magnetization increased with x up to 0.2 and then decreased with further doping 0.4, and coercivity values are increased with increasing concentration.

As can be seen, the saturation magnetization of undoped Co-Mg ferrite is ($x = 0.0$) 13.81 emu/g and

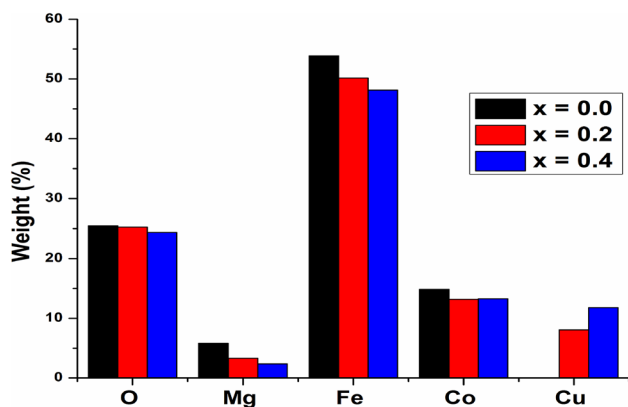


Fig. 5 Histogram for elemental weight composition of $\text{Co}_{0.5}\text{Mg}_{0.5-x}\text{Cu}_x\text{Fe}_2\text{O}_4$ nanoferrites

increases to a maximum value of 42.95 emu/g ($x = 0.2$), and then decreases for higher concentrations. Magnetization in nanoferrite is known to be strongly influenced by the site preference of the ions in the spinel lattice. So, Cu^{2+} ions are preferential to occupy the A-sites, while Co^{2+} and Mg^{2+} ions have a strong preference to occupy the B-sites. Fe^{3+} ions show preference for the B-sites. On further increasing the concentration of Cu in $\text{Co-Mg-Fe}_2\text{O}_4$ nanoferrite, it is due to the dopant Cu^{2+} ions, which prefers to occupy the octahedral sites pushing Fe^{3+} to the A-site, which in turn decreases the value of M_s . Similar variation in the result of magnetization is reported by others [33].

The initial permeability decreased for lower frequencies (1–50 MHz) and remained almost constant at a higher frequency (up to 50 MHz) with a copper concentration at room

Table 2 Conformation of elements of each sample of $\text{Co}_{0.5}\text{Mg}_{0.5-x}\text{Cu}_x\text{Fe}_2\text{O}_4$ analyzed by EDS

Composition	x = 0.0		x = 0.2		x = 0.4	
	Wt. %	At. %	Wt. %	At. %	Wt. %	At. %
O K	25.48	52.24	25.27	53.28	24.38	52.63
Mg K	5.82	7.85	3.31	4.59	2.38	3.38
Fe K	53.87	37.65	50.17	30.30	48.14	29.78
Co K	14.84	8.26	13.19	7.55	13.29	7.79
Cu K	—	—	8.06	4.28	11.81	6.42

Fig. 6 HRTEM images of $\text{Co}_{0.5}\text{Mg}_{0.5}\text{Fe}_2\text{O}_4$ nanoferrites a SAED pattern, b lattice planes, and c particle size

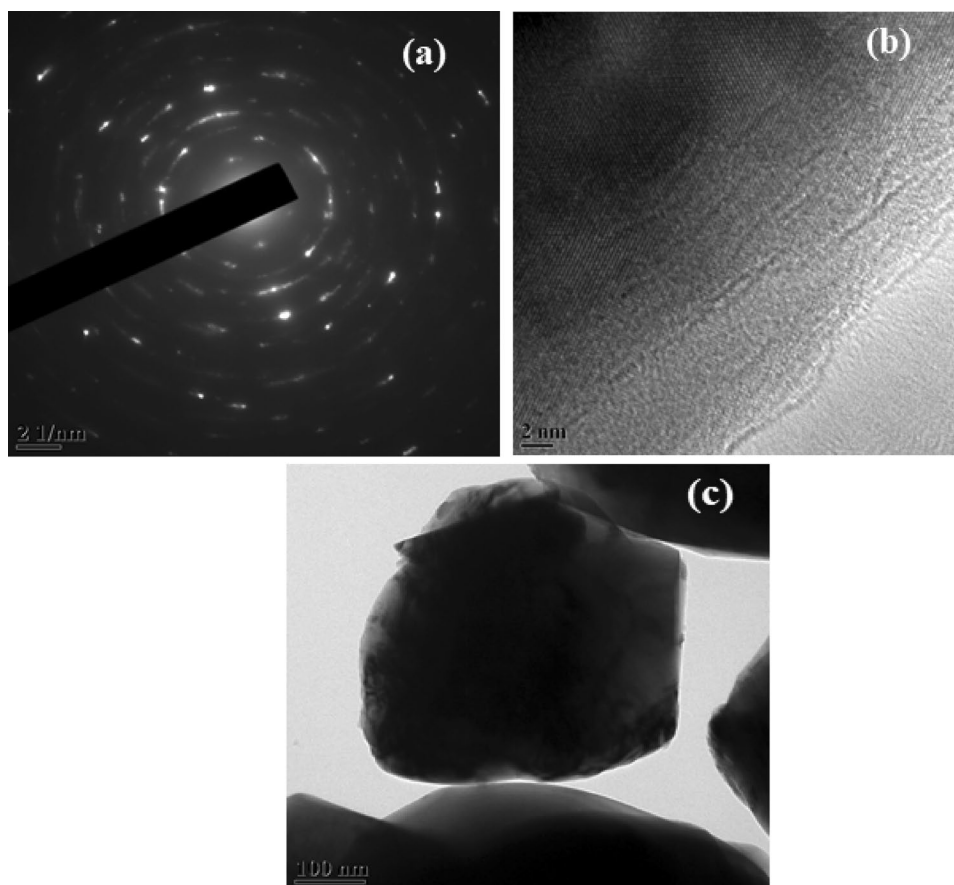
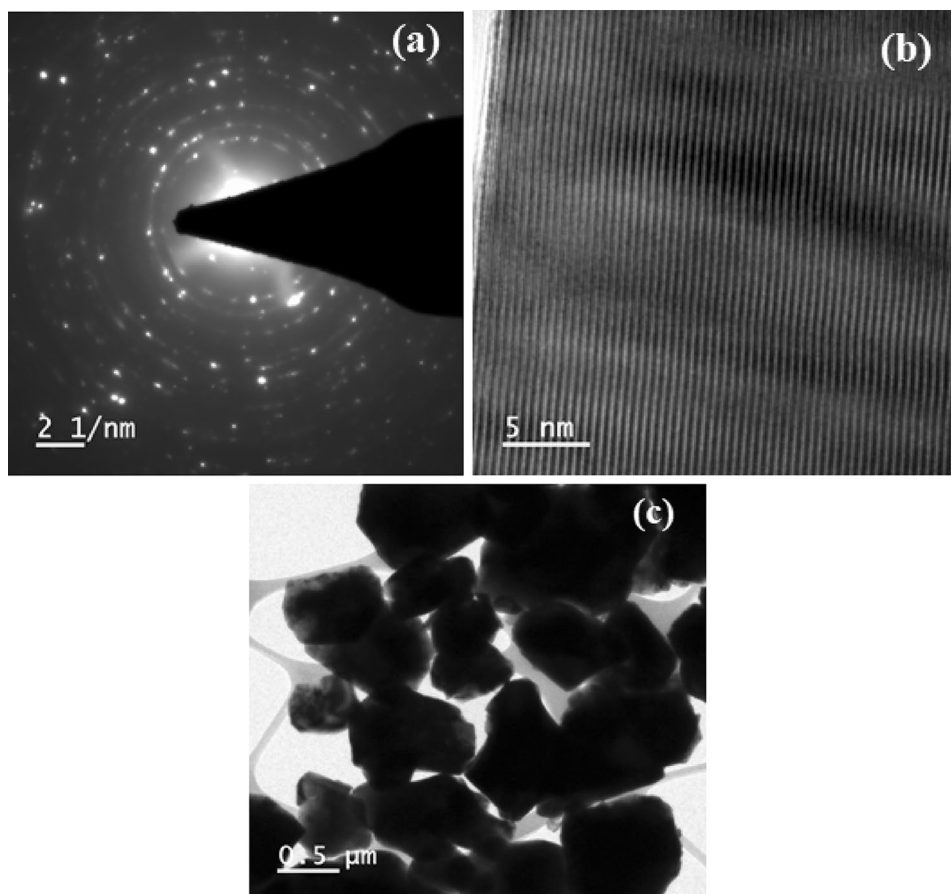


Fig. 7 HRTEM image of $\text{Co}_{0.5}\text{Mg}_{0.3}\text{Cu}_{0.2}\text{Fe}_2\text{O}_4$; **a** SAED pattern **b** lattice planes, and **c** particle size



temperature. Figure 11 shows the stability of the material at higher frequencies. This is the “utility region of ferrite” [34–36]. At lower frequencies, the increase in domain wall energy and spin rotation decreases the permeability irrespective of the saturation magnetization. The magnetic anisotropy, magnetostriction, and inner stress show the same behavior with permeability [37, 38]. Also, the sample’s permeability first increases and decreases with concentration, as shown in Fig. 12. The initial permeability is sensitive to many other parameters like magnetization, composition, grain size, anisotropy, etc. The Cu substitution changes the Fe^{3+} and Co^{2+} ion concentration at B-site.

The DC electrical resistivity ($\log \rho$) with Cu concentration at normal temperature is shown in Fig. 13. In the figure, the resistivity decreases with the increase in copper as copper is a good electricity conductor. The plot of temperature with dc electrical resistivity of $\text{Co}_{0.5}\text{Mg}_{0.5-x}\text{Cu}_x\text{Fe}_2\text{O}_4$ samples ($x=0.0, 0.2$ and 0.4) is shown in Fig. 14. The electrical resistivity decreases with an increase in the temperature, i.e., it has a negative temperature coefficient with resistance similar to semiconductors [20]. The influence of impurities or hopping of electrons increases conductivity at a lower temperature [39]. When fitted in the Arrhenius equation,

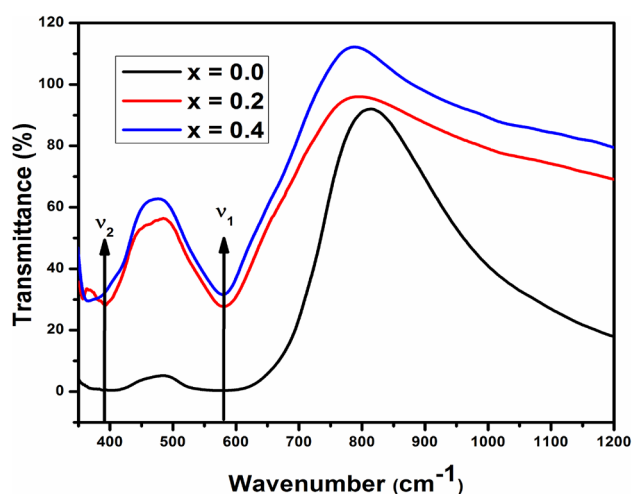


Fig. 8 Infrared spectra of $\text{Co}_{0.5}\text{Mg}_{0.5-x}\text{Cu}_x\text{Fe}_2\text{O}_4$ nanoferrites

the dc resistivity data give the electrons’ activation energy hopped with temperature. The equation is

$$\rho = \rho_0 e^{-\left(\frac{\Delta E}{KT}\right)} \quad (3)$$

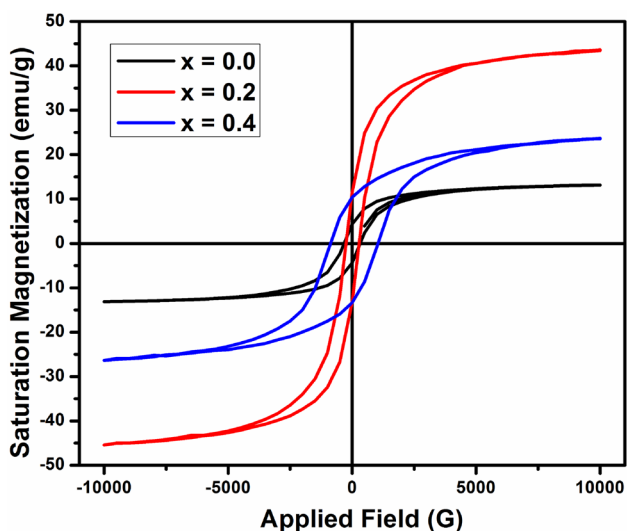


Fig. 9 Hysteresis loops of $\text{Co}_{0.5}\text{Mg}_{0.5-x}\text{Cu}_x\text{Fe}_2\text{O}_4$ nanoferrites at room temperature

Table 3 Tetrahedral (ν_1) and octahedral (ν_2) absorption bands and force constants (K_t, K_o) of $\text{Co}_{0.5}\text{Mg}_{0.5-x}\text{Cu}_x\text{Fe}_2\text{O}_4$ nanoferrites

Cu content (x)	ν_1 (cm^{-1})	K_t (dyne/cm)	ν_2 (cm^{-1})	K_o (dyne/cm)
0	587.32	1.39×10^5	401.91	4.76×10^4
0.2	580.23	1.31×10^5	357.09	6.62×10^4
0.4	585.58	1.45×10^5	389.84	5.88×10^4

where ρ is the dc electrical resistivity at temperature T , ρ_0 is the pre-exponential factor, ΔE is the activation energy, K is the Boltzmann constant and T is the absolute temperature. Change in activation energy for Cu concentration (x) of $\text{Co}_{0.5}\text{Mg}_{0.5-x}\text{Cu}_x\text{Fe}_2\text{O}_4$ samples is shown in Fig. 15.

The increase in Cu concentration or conductivity decreases the activation energy. This may be due to the formation of a few oxygen vacancies [40, 41].

Table 4 $M_s, M_r, H_c, \mu_{Bobs}, \mu_{Bth}$ and anisotropy constant (K) of $\text{Co}_{0.5}\text{Mg}_{0.5-x}\text{Cu}_x\text{Fe}_2\text{O}_4$ nanoferrites

Concentration (x)	M_s (emu/g)	M_r (emu/g)	H_c (Oe)	μ_{Bobs}	μ_{Bth}	$K(M_s H_c / 2)$ (erg/Oe)
0	13.81	4.24	321.06	0.49	6.13	4.39×10^3
0.2	42.95	12.4	264.14	1.79	5.5	1.20×10^4
0.4	23.64	11.9	959.65	1.04	5.14	2.45×10^4

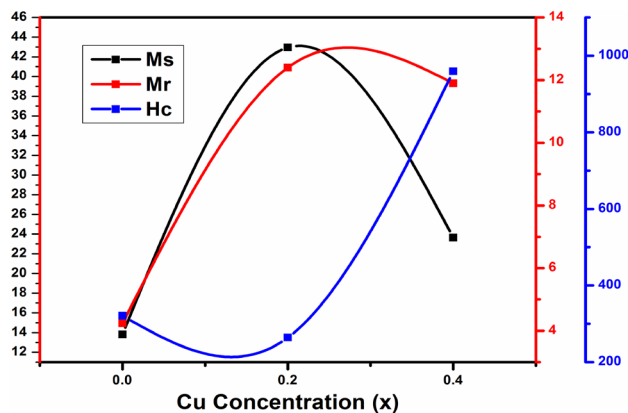


Fig. 10 Saturation magnetization (M_s), remnant magnetization (M_r), and coercivity (H_c) plot of $\text{Co}_{0.5}\text{Mg}_{0.5-x}\text{Cu}_x\text{Fe}_2\text{O}_4$ nanoferrites at room temperature

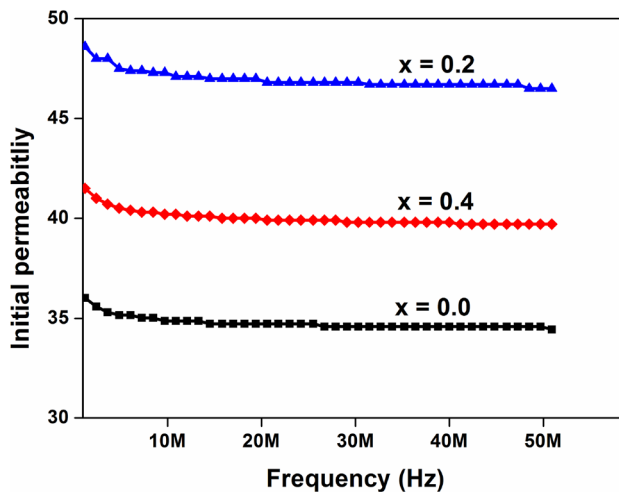


Fig. 11 Variation of initial permeability as a function of Cu concentration of $\text{Co}_{0.5}\text{Mg}_{0.5-x}\text{Cu}_x\text{Fe}_2\text{O}_4$ nanoferrites

4 Conclusions

Cu substituted mixed ferrites $\text{Co}_{0.5}\text{Mg}_{0.5-x}\text{Cu}_x\text{Fe}_2\text{O}_4$ ($x=0.0, 0.2$ and 0.4), and sample was manufactured with sol-gel method. The sharper peaks in XRD show the high crystalline character of the sample. Also, the peak shift toward the lower 2θ value with the increase in the concentration of Cu shows that the lattice parameter is

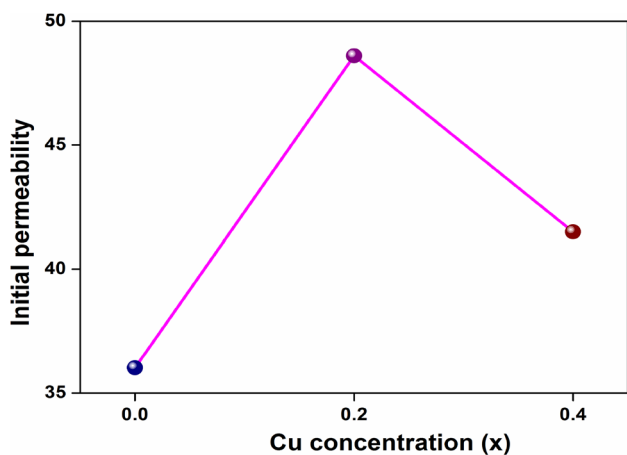


Fig. 12 Variation of initial permeability with Cu concentration for $\text{Co}_{0.5}\text{Mg}_{0.5-x}\text{Cu}_x\text{Fe}_2\text{O}_4$ nanoferrites

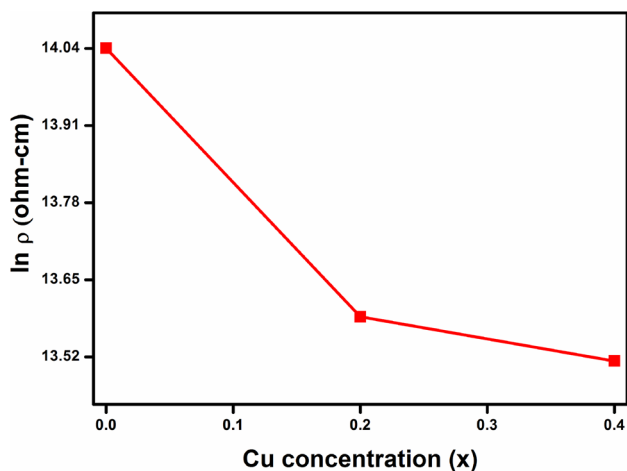


Fig. 13 Variation of room temperature DC resistivity as a function of $\text{Co}_{0.5}\text{Mg}_{0.5-x}\text{Cu}_x\text{Fe}_2\text{O}_4$ nanoferrites

increasing. Crystallite initially increases with Cu^{2+} concentration up to $x=0.2$ and then declines. This is the result of the non-uniform allocation of Mg and Cu ions. SEM analysis shows that the volume expanded by Cu of a larger ionic radius than Mg was overcome by its larger atomic weight and decreased density, resulting in decreased grain size. EDS analysis reaffirms O, Mg, Fe, Co, and Cu in the appropriate composition. The particle size calculated from HRTEM images by SAED pattern mode agreed well with the XRD values. The two strong absorption bands ν_1 with higher frequency and ν_2 with lower frequency in the FTIR curve show bond stretching $\text{M}_{\text{tetra}} \leftrightarrow \text{O}$ and $\text{M}_{\text{octa}} \leftrightarrow \text{O}$ (metal cation and oxygen) with respective force constants K_t and K_o in tetrahedral and octahedral positions, respectively. The remnant ratio ($R = M_t/M_o$) below

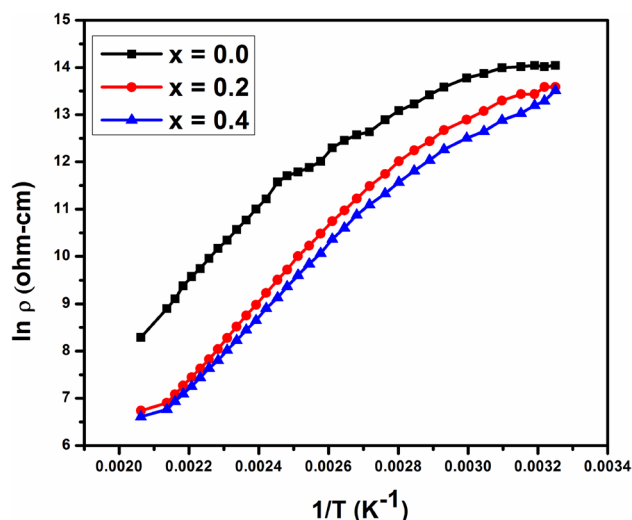


Fig. 14 Temperature Vs. DC electrical resistivity of $\text{Co}_{0.5}\text{Mg}_{0.5-x}\text{Cu}_x\text{Fe}_2\text{O}_4$ nanoferrites

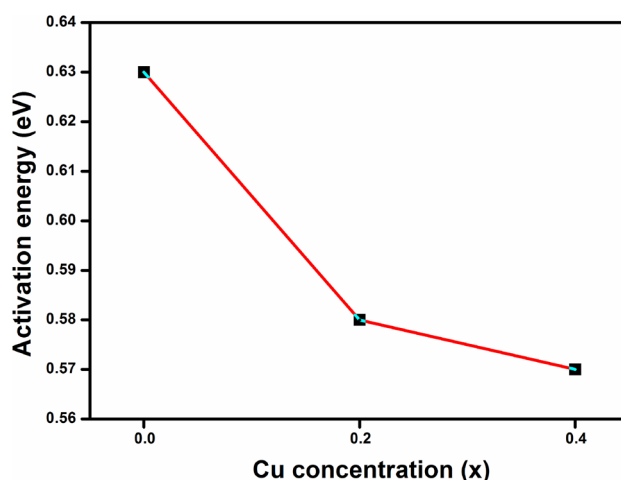


Fig. 15 Activation energy Vs. Cu concentration(x) of $\text{Co}_{0.5}\text{Mg}_{0.5-x}\text{Cu}_x\text{Fe}_2\text{O}_4$ nanoferrites

0.5 shows the isotropic nature of the materials forming single domain ferrimagnetic particles. The permeability of the sample varies at lower frequencies and is stable at high frequency. This stability region is the zone of the utility of the ferrite. DC resistivity decreases with an increase in the copper content as copper is a good conductor of electricity. The electrical resistivity decreases with an increase in the temperature, i.e., it has a negative temperature coefficient with resistance similar to semiconductors. The increase in Cu concentration or conductivity decreases the activation energy. This is due to the formation of a few oxygen vacancies.

References

1. A. Ramakrishna, N. Murali, S.J. Margarete, K. Samatha, V. Veeraiah, *Physica B: Condens. Matter* **530**, 251–257 (2018)
2. P. Jadoun, J. Sharma, S. Kumar, S.N. Dolia, D. Bhatnagar, V.K. Saxena, *Ceram. Int.* **44**, 6747–6753 (2018)
3. A. Ramakrishna, N. Murali, S.J. Margarete, T.W. Mammo, N. Krishna Joythi, B. Sailaja, Ch.C. Sailaja Kumari, K. Samatha, V. Veeraiah, *Adv. Powder Technol.* **29**, 2601–2607 (2018)
4. A. Ramakrishna, N. Murali, T.W. Mammo, K. Samatha, V. Veeraiah, *Physica B: Condens. Matter* **534**, 134–140 (2018)
5. S. J. Mercy, D. Parajuli, N. Murali, A. Ramakrishna, Y. Ramakrishna, V. Veeraiah, K. Samatha, *Appl. Phys. A-Mater. Sci. Process.* **127**(2), 1–13 (2021)
6. P.P. Hankare, R.P. Patil, K.M. Garadkar, R. Sasikala, B.K. Chougule, *Mater. Res. Bull.* **46**, 447–452 (2011)
7. P. Himakar, N. Murali, D. Parajuli, V. Veeraiah, K. Samatha, T.W. Mammo, K.M. Batoo, M. Hadi, E.H. Raslan, S.F. Adil, *J. Electron. Mater.* 1–9 (2021)
8. M. Kurian, S. Thankachan, D.S. Nair, E.K. Aswathy, A. Babu, A. Thomas, K.T. Binu Krishna, *J. Adv. Ceram.* **4**(3), 199–205 (2015)
9. S. Yonatan Mulushoa, N. Murali, M. Tulu Wegayehu, S.J. Margarete, K. Samatha, *Results Phys.* **8**, 772–779 (2018)
10. R.C. Kambale, P.A. Shaikh, C.H. Bhosale, K.Y. Rajpure, Y.D. Kolekar, *Smart Mater. Struct.* **18**(115028), 1–7 (2009)
11. M. Ghanbari, F. Ansari, M. Salavati-Niasari, *Inorg. Chim. Acta.* **455**, 88–97 (2017)
12. F. Ansari, A. Sobhani, M. Salavati-Niasari, *J. Colloid Interface Sci.* **514**, 723–732 (2018)
13. C. Nlebedim, K.W. Dennis, R.W. McCallum, D.C. Jiles, *J. Appl. Phys.* **115**, 17A519 (2014)
14. N. Murali, S.J. Margarete, G.P. Kumar, B. Sailaja, S.Y. Mulushoa, P. Himakar, B. K. Babu, V. Veeraiah, *Phys. B: Condens. Matter* **522**, 1–6 (2017)
15. H. S. Mund, B. L. Ahuja, *Mater. Res. Bull.* (2017) 228–233.
16. J.B. Nelson, D.P. Riley, *Proc Phys Soc.* (1926–1948) **57**(3), 160–177 (1945)
17. C.O. Ehi-Eromosele, B.I. Ita, E.E.J. Iweala, *J. Sol-Gel, Sci. Technol.* **76**, 298–308 (2015)
18. A. Monshi, M.R. Foroughi, M.R. Monshi, *World J. Nano Sci. Eng.* **2**, 154–160 (2012)
19. B.P. Jacob, S. Thankachan, S. Xavier, E.M. Mohammed, *Phys. Scr.* **84**, 045702 (2011)
20. S.S. Abbas, I.H. Gul, S. Ameer, M. Anees, *Electron. Mater. Lett.* **11**, 100–108 (2015)
21. M.A. Khan, M.A. MuIslam, M. Iqbal, M.F. Ahmad, G. Din, I. Murtaza, M.F. Ahmad, Warsi, *Magnetic. Ceram. Int.* **40**, 3571–3577 (2014)
22. A. Hassan, M. Azhar Khan, M. Shahid, M. Asghar, I. Shakir, S. Naseem, S. Riaz, M. Farooq Warsi, *J. Magn. Magn. Mater.* **393**, 56–61 (2015)
23. T.W. Mammo, C.H. Vijaya Kumari, S.J. Margarete, A. Ramakrishna, R. Vemuri, Y.B. Shankar Rao, K.L. Vijaya Prasad, Y. Ramakrishna, N. Murali, *Physica B: Condensed Matter* **581**, 411769 (2020)
24. A. Ghasemi, A. Hossienpour, A. Morisako, A. Saatchi, M. Salehi, *J. Magn. Magn. Mater.* **302**, 429–435 (2006)
25. L. Fernandez-Barquin, M.V. Kuznetsov, Y.G. Morozov, Q.A. Pankhurst, I.P. Parkin, *Int. J. Inorg. Mater.* **1**, 311–316 (1999)
26. N. Hari Kumar, G. Aravind, D. Ravinder, T. Somaiah, B. Ravinder Reddy, *Int. J. Eng. Res. Appl.* **4**, 137–141 (2014)
27. M. AsifIqbal, M. Islam, I. Ali, M.A. Khan, S.M. Ramay, M.H. Khan, M.K. Mehmood, *J. Alloy. Comp.* **692**, 322–331 (2017)
28. Y. Li, R. Liu, Z. Zhang, C. Xiong, *Mater. Chem. Phys.* **64**, 256–259 (2000)
29. M. U. Islam, I. Ahmad, T. Abbas, M. A. Chaudhry, R. Nazmeen, *Advanced Materials, In: Proceedings of the 6th International Symposium* (1999) 155.
30. L.G.V. Uitert, *J. Chem. Phys.* **24**, 306–310 (1956)
31. A.A. Samokhralov, A.G. Rustmov, *Sov. Phys. Solid State* **7**, 961 (1965)
32. N.M. Deraz, A. Alarifi, *Int. J. Electrochem. Sci.* **7**, 5534–5543 (2012)
33. A. Amirabadizadeh, T. Amirabadi, *World J. Condens. Matter. Phys.* **3**, 131–135 (2013)
34. T.W. Mammo, N. Murali, Y.M. Sileshi, T. Arunamani, *Physica B* **531**, 164–170 (2018)
35. A. Verma, T.C. Goel, R.G. Mendiratta, R.G. Gupta, *J. Magn. Magn. Mater.* **192**, 271–276 (1999)
36. R.H.R. Khana, A.K.M. Akther Hossainb, *J. Magn. Magn. Mater.* **324**, 550–558 (2012)
37. C.H. Sumatra, K. Venugopal Reddy, K. Sowri Babu, A. Rama Chandra Reddy, M. Buchi Suresh, K.H. Rao, *J. Magn. Magn. Mater.* **340**, 38–45 (2013)
38. B.S. Trivedi, N.N. Jani, H.H. Joshi, R.G. Kulkarni, *J. Mater. Sci.* **35**, 5523–5526 (2000)
39. V. Raghavendra, G. Raju, M. Gnana Kiran, M.S.N.A. Prasad, E. Rajesh, G. Pavan Kumar, N. Murali, *Results Phys.* **12**, 947–952 (2019)
40. B. Shinde, *Int. J. Res. Eng. Appl. Sci.* **6**(3), 5–77 (2016)
41. S.A. Mazen, N.I. Abu-Elsaad, *Appl. Nanosci.* **5**, 105–114 (2015)

Publisher's Note Springer Nature remains neutral with regard to jurisdictional claims in published maps and institutional affiliations.